J. Fluid Mech. (2015), *vol.* 780, *pp.* 687–716. © Cambridge University Press 2015
doi:10.1017/jfm.2015.479

Long-wave instability of a helical vortex

Hugo Umberto Quaranta[1,2], Hadrien Bolnot[1,2] and Thomas Leweke[1,†]

[1]IRPHE UMR 7342, Aix-Marseille Université, CNRS, Centrale Marseille, 13384 Marseille, France
[2]Aerodynamics Department, Airbus Helicopters, 13725 Marignane, France

(Received 4 February 2015; revised 29 July 2015; accepted 10 August 2015;
first published online 9 September 2015)

We investigate the instability of a single helical vortex filament of small pitch with respect to displacement perturbations whose wavelength is large compared to the vortex core size. We first revisit previous theoretical analyses concerning infinite Rankine vortices, and consider in addition the more realistic case of vortices with Gausssian vorticity distributions and axial core flow. We show that the various instability modes are related to the local pairing of successive helix turns through mutual induction, and that the growth rate curve can be qualitatively and quantitatively predicted from the classical pairing of an array of point vortices. We then present results from an experimental study of a helical vortex filament generated in a water channel by a single-bladed rotor under carefully controlled conditions. Various modes of displacement perturbations could be triggered by suitable modulation of the blade rotation. Dye visualisations and particle image velocimetry allowed a detailed characterisation of the vortex geometry and the determination of the growth rate of the long-wave instability modes, showing good agreement with theoretical predictions for the experimental base flow. The long-term (downstream) development of the pairing instability leads to a grouping and swapping of helix loops. Despite the resulting complicated three-dimensional structure, the vortex filaments surprisingly remain mostly intact in our observation interval. The characteristic distance of evolution of the helical wake behind the rotor decreases with increasing initial amplitude of the perturbations; this can be predicted from the linear stability theory.

Key words: vortex flows, vortex instability, vortex interactions

1. Introduction

Vortex filaments are basic ingredients of transitional and turbulent flows and the study of their fundamental dynamics and interactions may help understand the behaviour of the often complicated flows encountered in nature or industry. Along with pairs and arrays of straight vortices and vortex rings, an infinite helical filament is one of the elementary vortex configurations that have been considered in the past. It is the simplest geometry combining the effects of mutual induction (between neighbouring helix turns) and self-induced motion due to the curvature and torsion of the filament. It has the special property of preserving its shape under its own influence (Kida 1981), which results in a 'rigid' translation and rotation. Helical

† Email address for correspondence: leweke@irphe.univ-mrs.fr

vortices may arise in various situations, e.g. from the destabilisation of an initially straight vortex (Ash & Khorrami 1995), in particular when there is an axial flow present in the core, or from the instability of a round jet (Koch *et al.* 1989). A specific application is the modelling of the flow around rotors, whose near and intermediate wake consists of a system of interlaced helical vortices generated at the rotor blade tips. Examples include ship propellers (Felli, Camussi & Felice 2011), helicopters (Leishman 2006) and horizontal-axis wind turbines (Vermeer, Sørensen & Crespo 2003). The stability properties of these flows have practical relevance: for wind turbines, the tip vortex instabilities contribute to the transition from an organised vortex system to a turbulent wake behind the rotor (Sørensen *et al.* 2014), and they may be related to the inception of the dangerous vortex ring state of the wake of a helicopter in steep descent (Leishman, Bhagwat & Ananthan 2004; Bolnot, Le Dizès & Leweke 2014).

The stability of helical vortex systems has been analysed theoretically by a number of authors. These studies can be divided into two groups according to the type of vortex interaction considered for the stability analysis (Leweke *et al.* 2014). One mechanism involves perturbations displacing the vortices locally as a whole, i.e. without change of their core structure, with wavelengths that are large compared to the core radius. A second mechanism is linked to the amplification of short-wave perturbations inside the vortex cores. The growth of these modes is due to the modification of the core structure by an external strain field, induced, e.g. by a second nearby vortex, or by the curvature and torsion of the vortex. These effects produce the so-called elliptic instability (Kerswell 2002) or curvature instability (Fukumoto & Hattori 2005; Hattori & Fukumoto 2009).

The present work concerns the long-wavelength displacement instability, for which the vortices can be approximated by filaments whose shapes evolve under the effect of their mutually- and self-induced velocities. Betchov (1965) and Kida (1982) studied the stability of a single helical vortex using the local-induction approximation, where the velocity of a point on the filament depends only on the local curvature. This approach is appropriate for helices with large pitch (nearly-straight vortices). Instability was found for long-wavelength perturbations. Widnall (1972) included the effects of the entire filament on the self-induced velocity through the Biot–Savart line integral associated with the cutoff method (Crow 1971) to avoid its singularity (a much earlier study by Levy & Forsdyke (1928) of the same configuration was shown to be erroneous). Additional modes of instability were found for small pitch, when successive helix turns are close enough to interact significantly. The most unstable perturbations are those for which the displacements of neighbouring turns are out of phase. Fukumoto & Miyazaki (1991) extended this work by considering an axial flow along the vortex core, which was found to suppress the instability for certain configurations with large pitch. Gupta & Loewy (1974), and later Okulov & Sørensen (2007), considered systems of several interlaced helices, in the latter case also including a straight central vortex which models the hub vortex of a rotor wake. Again, the most unstable perturbations involve out-of-phase displacements between successive vortex loops. Interestingly, a similar behaviour is found for an infinite array of vortex rings (Levy & Forsdyke 1927; Bolnot *et al.* 2014), whose geometry for small separations is close to a helix with small pitch.

Evidence of the instability modes predicted by the above theories can be found in a number of numerical and experimental studies, mostly dedicated to the investigation of rotor wakes. Bhagwat & Leishman (2000) and Leishman *et al.* (2004) have calculated the vortex wake of a hovering helicopter using a free vortex method.

The stability analysis of these configurations showed qualitatively the same unstable modes and growth rate curves as in Widnall (1972) and Gupta & Loewy (1974). More recently, Walther *et al.* (2007) have simulated several of these modes using a vortex method. Similar observations were reported by Ivanell *et al.* (2010) and Sarmast *et al.* (2014), who have used the actuator line method (Sørensen & Shen 2002) to simulate the wake of a three-bladed wind turbine. Laboratory experiments with models of ship propellers (Felli *et al.* 2011), helicopter rotors (Stack, Caradonna & Savaş 2005; Ohanian, McCauley & Savaş 2012) and wind turbines (Alfredsson & Dahlberg 1979; Sherry *et al.* 2013; Naumov *et al.* 2014; Nemes *et al.* 2015) exhibit 'grouping', 'leapfrogging' and 'merging' of the helical wake vortices, which are all manifestations of the pairing instability predicted by Widnall (1972). Nevertheless, a precise quantitative comparison between experimental and theoretical results is still lacking; it is one of the objectives of the present work to fill this gap.

This paper deals with the long-wave displacement instability of a single helical vortex of moderate pitch (less than one helix radius). In the following, we first review the main theoretical results from the work of Widnall (1972) and Gupta & Loewy (1974) concerning this phenomenon, including some minor corrections and an extension from the Rankine vortex model (constant-vorticity core) used in these studies, to a more realistic Gaussian vorticity model with an additional axial core flow. Building upon the observed phase relation of the unstable perturbation, we establish a quantitative link with the classical pairing instability of an infinite row of point vortices in two dimensions (see, e.g. Lamb 1932, § 156). We then present a detailed experimental study of a single helical vortex generated by a one-bladed rotor in water. The control of the blade rotation was used to select the different instability modes individually, in order to visualise them clearly and to determine their growth rates. Together with the full set of base flow parameters, this allows a meaningful quantitative comparison with theoretical predictions. The nonlinear evolution of the perturbed vortex, as it moves downstream, is also discussed.

2. Theoretical background

2.1. *Helical vortex configuration*

We consider an infinite helical vortex filament in a cylindrical reference frame (r, θ, z), as depicted in figure 1, which represents a simplified model of the wake behind the single-bladed rotor used in the experiments described in §§ 3–6. The helix geometry is defined by the radius R and the pitch h of the vortex centre line, whose coordinates $\boldsymbol{r_h}$ are

$$\boldsymbol{r_h} = \begin{pmatrix} r_h \\ \theta_h \\ z_h \end{pmatrix} = \begin{pmatrix} R \\ \theta \\ h\theta/2\pi \end{pmatrix}; \quad \theta \in \mathbb{R}. \tag{2.1}$$

R and h are both considered as constant. Additional parameters are the vortex circulation Γ and the core radius a.

The structure of the filament is further characterised by the distributions of azimuthal and axial velocities in the local cylindrical reference frame (ρ, ϕ, ξ) of the vortex (see figure 2), which are axisymmetric at leading order. Previous theoretical studies have mostly considered Rankine-type vortices, with constant vorticity inside the core, zero vorticity outside and without axial flow. In the present analysis, we allow for a more realistic smoother vorticity (and swirl velocity) profile, as well as an axial core flow, as shown in figure 2. One model which includes these features

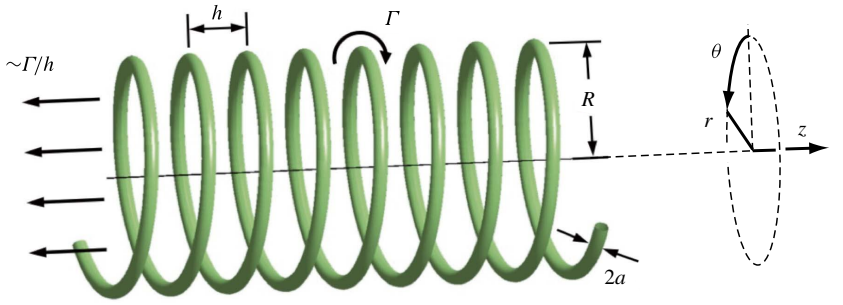

FIGURE 1. (Colour online) Schematic of an infinite helical vortex including the relevant parameters: pitch h, radius R, core size a and circulation Γ.

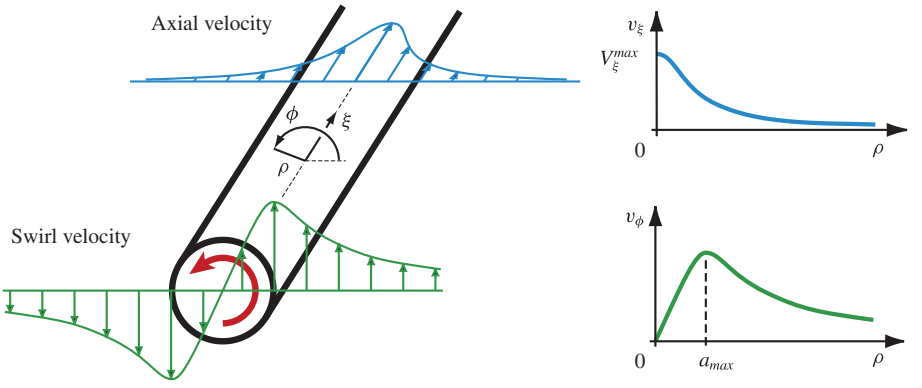

FIGURE 2. (Colour online) Schematic of the azimuthal (ϕ) and axial (ξ) velocity profiles of the vortex.

is the Batchelor vortex with a Gaussian vorticity distribution, whose azimuthal and axial velocities are respectively given by

$$v_\phi(\rho) = \frac{\Gamma}{2\pi\rho}[1 - \exp(-\rho^2/a^2)] \quad \text{and} \quad v_\xi(\rho) = V_\xi^{max} \exp(-\rho^2/a^2). \tag{2.2a,b}$$

The core radius a in this model is related to the radius a_{max} of maximum swirl velocity (see figure 2), which can easily be determined from experimental measurements, by the relation

$$a_{max} \approx 1.12\, a. \tag{2.3}$$

The non-dimensional parameters describing a helical vortex with a structure given by (2.2) are the Reynolds number $Re = \Gamma/\nu$ (ν: kinematic viscosity), the scaled pitch h/R and core radius a/R and an axial flow parameter

$$W = 2\pi a V_\xi^{max}/\Gamma, \tag{2.4}$$

representing the ratio between maximum axial velocity and maximum swirl velocity. It is equivalent to an inverse swirl number. Typical parameter values for the present study are: $Re = 10^4$; $h/R = 0.5$; $a/R = 0.05$; and $W = 0.5$. For an infinite helical vortex,

the fluid velocities in the direction z of the axis of symmetry differ by an amount Γ/h between the inside and the outside of the cylinder containing the helix. In a reference frame where the z-velocity vanishes at large r, the helix is convected with a velocity of approximately $\Gamma/2h$ (a small difference comes from the self-induced motion due to the vortex curvature). In the following, the pitch h and the velocity $\Gamma/2h$ are used for normalisation. In particular, the time $2h^2/\Gamma$ is used to obtain non-dimensional instability growth rates. It corresponds roughly to the time it takes the helix to move one pitch in the axial direction under its own influence.

In order to be able to use previous theoretical results for Rankine vortices, we recall the concept of an equivalent core size first introduced by Widnall, Bliss & Zalay (1971). The distributions of azimuthal and axial velocity have an effect on the self-induced motion of the vortex. It can be shown that, for long-wave displacement perturbations such as the ones considered in the present work, the self-induced dynamics of a vortex with velocity profiles $v_\phi(\rho)$ and $v_\xi(\rho)$, evolving on a characteristic radial scale a, exhibit the same self-induced dynamics as an equivalent Rankine vortex without axial flow, with the same circulation and a core radius given by

$$a_e = a\exp\left[\tfrac{1}{4} - A + C\right], \quad \text{where} \tag{2.5}$$

$$A = \lim_{\rho\to\infty}\left[\frac{4\pi^2}{\Gamma^2}\int_0^\rho \rho' v_\phi^2(\rho')\,\mathrm{d}\rho' - \ln\frac{\rho}{a}\right] \quad \text{and} \quad C = \frac{8\pi^2}{\Gamma^2}\int_0^\infty \rho' v_\xi^2(\rho')\,\mathrm{d}\rho'. \tag{2.6a,b}$$

For the Batchelor vortex (2.2) one finds

$$a_e = a\sqrt{2}\exp\left[\frac{1}{4} - \frac{\gamma}{2} + \frac{W^2}{2}\right] \approx 1.36\,a\,\exp\left(\frac{W^2}{2}\right). \tag{2.7}$$

$\gamma \approx 0.577$ is Euler's constant. Equation (2.7), together with (2.3), is used in § 3 for the comparison between experimental and theoretical results (the fact that the experimental vortex is not exactly Gaussian is discussed in § 4).

2.2. *Displacement instability*

In its unperturbed base state, the helical vortex rotates around its axis and translates in the direction of this axis due to its self-induced velocity, without changing shape. The stability of this configuration is analysed by considering the evolution of displacement perturbations of the base geometry in (2.1). Following Widnall (1972) and Gupta & Loewy (1974), perturbations of the form

$$\delta\boldsymbol{r_h} = \begin{pmatrix}\delta r_h\\ \delta\theta_h\\ \delta z_h\end{pmatrix}\exp(\alpha t + \mathrm{i}k\theta_h), \tag{2.8}$$

with azimuthal wavenumber k and (complex) growth rate α, are considered. The evolution of the filament shape is obtained by computing its self-induced velocity from the Biot–Savart law. For a vortex of small core size, the velocity $\boldsymbol{u}$ induced at a point $\boldsymbol{r_0}$ in the fluid is given by

$$\boldsymbol{u}(\boldsymbol{r_0}) = \frac{\Gamma}{4\pi}\int \frac{[\boldsymbol{r_0} - \boldsymbol{r}(l)]\times \mathrm{d}\boldsymbol{l}}{|\boldsymbol{r_0} - \boldsymbol{r}(l)|^3}, \tag{2.9}$$

where l is the curvilinear coordinate along the vortex centre line. For a point on this line, i.e. $\boldsymbol{r_0} = \boldsymbol{r}(l_0)$, the integral in (2.9) diverges, and the detailed core structure has to be taken into account in order to determine the correct self-induced velocity. Widnall (1972) employed the cutoff method, in which the interval $l_0 - \varepsilon < l < l_0 + \varepsilon$ containing the singularity is excluded from the integration. For a Rankine vortex with core radius a_e and without axial flow, the correct cutoff distance is given by $\varepsilon = (a_e/2)\exp(1/4)$. Gupta & Loewy (1974) used a different approach, initially proposed by Rosenhead (1930), to desingularize the integrand in (2.9). The denominator is replaced by $|[\boldsymbol{r_0} - \boldsymbol{r}(l)]^2 + \mu^2|^{3/2}$, where μ is a length proportional to the core size. If $\mu = (2/e)\varepsilon = a_e \exp(-3/4) \approx 0.47 a_e$, this procedure is equivalent to the cutoff method (Saffman 1992). Gupta & Loewy (1974), however, used $\mu = a_e$, which explains the discrepancies with Widnall's (1972) results for large core size.

Linearisation of the evolution equations for the perturbed helix shape, using one or the other adapted versions of (2.9), then leads to an eigenvalue problem for the growth rate α, whose real part σ characterises the growth or decay of the perturbation amplitude. The corresponding eigenvectors $(\delta r_h,\ \delta\theta_h,\ \delta z_h)$ define the mode shape. Details of the calculations can be found in Widnall (1972) and Gupta & Loewy (1974). Figure 3 shows an example of the non-dimensional growth rate $\sigma^* = \sigma(2h^2/\Gamma)$ as a function of the perturbation wavenumber k. It corresponds to one of the cases discussed by Widnall (1972), with values of the helix pitch and core size close to the ones considered in the present study. The difference between Widnall's analytical result and the corresponding figure in her paper is believed to be due to the difficulties (at the time) in numerically evaluating the rather complex functions and integrals appearing in the expression of the growth rate, or simply to a plotting error. The growth rate has local maxima for wavenumbers which are odd multiples of $1/2$. The highest growth rate is obtained for $k = 1/2$, its value is close to $\sigma^* = \pi/2$.

The theoretical development by Widnall (1972) assumes that the wavelength of the displacement perturbations is large compared to the core size, which corresponds to an upper limit of validity for the (dimensional) wavenumber k_l along the vortex centre line. Leweke & Williamson (1998) have estimated this limit for a straight Rankine vortex of radius a_e, based on the exact dispersion relation for perturbation waves of such a vortex (Kelvin waves), to be $k_l a_e \approx 0.4$. This result can be used to estimate the range of validity of the theory for the helical geometry. From the definition of the non-dimensional wavenumber k (= number of perturbation wavelengths in one helix turn of length $L = [h^2 + (2\pi R)^2]^{1/2}$), it is straightforward to show that the long-wave condition corresponds to

$$k \lesssim \frac{(a_e/R)^{-1}}{5\pi}\sqrt{(h/R)^2 + 4\pi^2}. \tag{2.10}$$

For the case shown in figure 3 ($a_e/R = 0.1$), one obtains $k \lesssim 4.0$ (for $a_e/R = 0.33$, the range of validity is even reduced to $k \lesssim 1.2$, but this configuration is unrealistic since successive helix turns have overlapping cores). In the experimental study presented in § 3, we observe very thin-cored vortices ($a_e/R \approx 0.05$), for which the limit of validity of the long-wave theory is not a concern.

The effect of viscosity was neglected in the above analysis. The correction of the growth rate due to viscous damping can be estimated to be of the order of $-\nu k_l^2$, which in non-dimensional form equals $-(8\pi^2/Re)k^2(h/L)^2$. For the parameter ranges considered in this study ($h/R < 1$, $k < 4$, $Re = O(10^4)$), the non-dimensional viscous

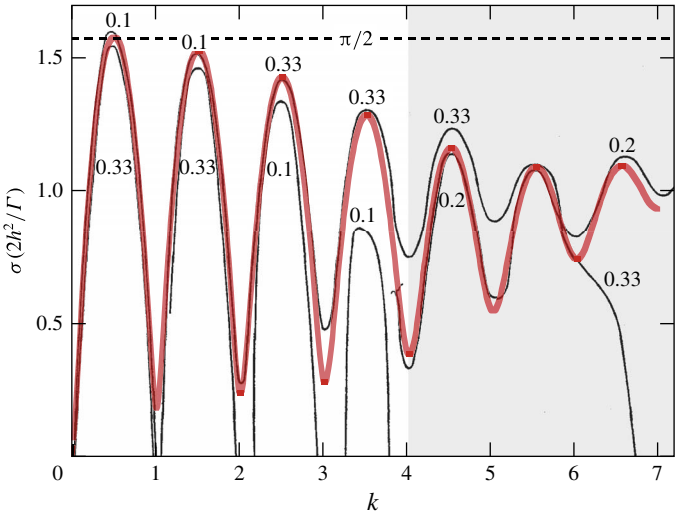

FIGURE 3. (Colour online) Growth rate as function of wavenumber for a helical Rankine vortex with $h/R = \pi/5$. Black (thin) lines: figure 5(*d*) from Widnall (1972), the numbers indicate a_e/R (reproduced with permission); red (thick) line: analytical result from Widnall (1972) for $a_e/R = 0.1$. The long-wave assumption used in the theory is not valid in the shaded area.

correction is of $O(10^{-2})$ and will therefore not be considered further here (for full-scale applications such as wind turbines, where the Reynolds number is several orders of magnitudes larger, viscous effects on the pairing instability are even less relevant).

The instability growth rates obtained with the formalism of Gupta & Loewy (1974), using the correct parameter μ, are identical to the ones from Widnall's (1972) analysis, within the range of validity of the theory. For the comparison with our experimental measurements, we use the former procedure, which is appreciably easier to implement.

Figure 4 presents two examples of deformations of the initially helical vortex due to the displacement instability by plotting the perturbed helix geometry $\boldsymbol{r_h} + \delta\boldsymbol{r_h}$ ((2.1) and (2.8)). The perturbation $\delta\boldsymbol{r_h}$ is the unstable eigenmode corresponding to the given wavenumber k. Figure 4(*a*) shows one of the most unstable perturbations, for $k = 3/2$. For this value of the wavenumber, as for all odd multiples of $1/2$, the displacement perturbations of successive helix loops are exactly out of phase at a given azimuthal position θ. The developed plan view reveals that these perturbations correspond to a local pairing of neighbouring helix turns, with the pattern repeating after two turns. For wavenumbers away from the local maxima of the growth rate curve, e.g. for $k = 4/3$ in figure 4(*b*), the perturbation repeats at constant θ after a longer period, but a local grouping of two successive helix loops is still found at various azimuthal positions. One can easily work out that a perturbation with a wavenumber of the form $k = m/n$ repeats after n cycles and exhibits m azimuthal locations where local grouping occurs. Further examples of unstable perturbation modes can be seen in figures 17 and 18.

2.3. *Pairing of vortex arrays*

As seen in the previous section, the long-wave displacement instability of a helical vortex is characterised by a periodic local pairing of successive turns. This is further

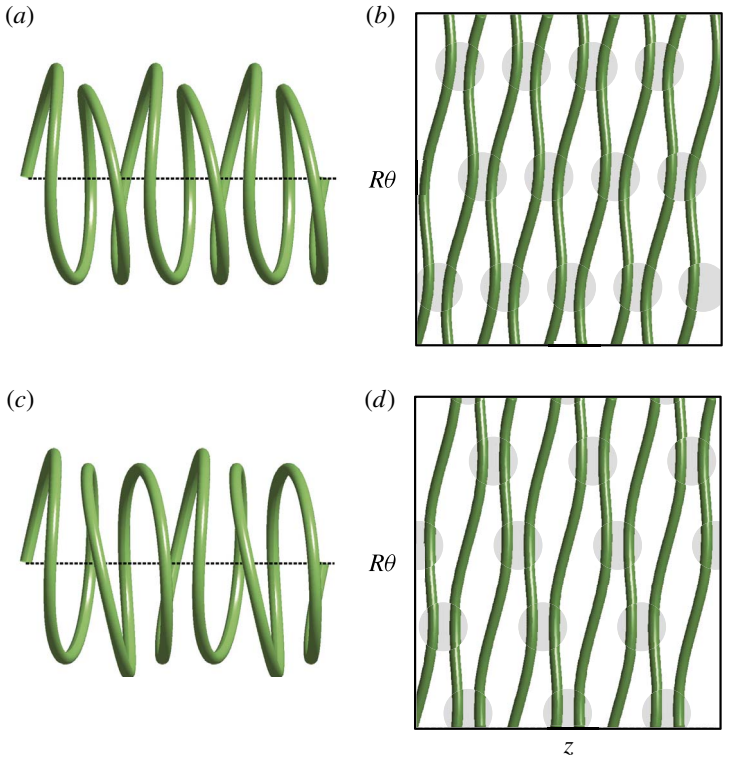

FIGURE 4. (Colour online) Geometrical deformation and local paring predicted by Widnall (1972) for the case $h/R = 0.5$. (*a*,*b*) $k = 3/2$; (*c*,*d*) $k = 4/3$. Three-dimensional view (*a*,*c*) and developed plan view (*b*,*d*). The vertical scale of the plan views is compressed by a factor 2.

illustrated by considering a longitudinal plane containing the helix axis. In this plane, the helical vortex appears in the form of two periodic rows of concentrated vortices (see, e.g. figure 21). These rows bear a resemblance to arrays of point vortices in two dimensions, which are also known to be unstable with respect to the pairing mechanism. In addition to this qualitative similarity, we now establish a quantitative link between the helix instability and the classical pairing of a point vortex array.

The stability of an infinite row of identical point vortices was treated by Lamb (1932) based on earlier work by von Kármán & Rubach (1912). The vortices of circulation Γ are separated by a constant distance b from their next neighbours, and this base configuration is stationary. The position of each vortex is then perturbed periodically along the array, with a phase difference Φ for the displacements of two adjacent vortices. It is found that the array is unstable for all perturbations with non-zero Φ ($\Phi = 0$ corresponds to a neutral translation of the entire row), and that the instability growth rate σ_p is given by:

$$\sigma_p(\Phi) = \frac{\Gamma}{4\pi b^2}\Phi(2\pi - \Phi). \tag{2.11}$$

The maximum is reached for $\Phi = \pi$, i.e. for out-of-phase displacements of neighbouring vortices, which corresponds to the pairing shown schematically in

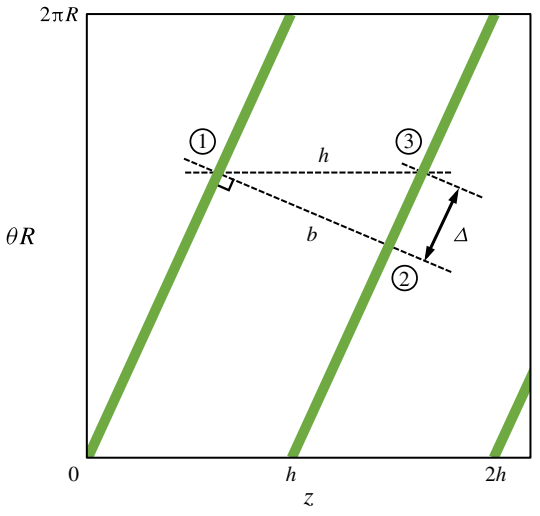

FIGURE 5. (Colour online) Schematic of the developed plan view of the helix, showing the parameters used in the analysis.

figure 21(*b*). The growth rate for this case is $\sigma_p = \pi\Gamma/4b^2$ or, in non-dimensional form, $\sigma_p(2b^2/\Gamma) = \pi/2$.

We now transpose this result to the case of a helical vortex by considering the developed plan view of this configuration in figure 5. In this representation, the helix appears as a periodic array of inclined straight vortices that can be associated with a row of point vortices in a plane going through ① and ②. From the form of the perturbations of the helix instability in (2.8), the phase difference between ① and ③, separated by a complete turn, equals $2\pi k$. The phase difference Φ between ① and ② is reduced from this value by a fraction Δ/L, where L is again the length of one helix turn. The geometrical relations in figure 5 lead to $\Delta = h^2/L$, and therefore:

$$\Phi = 2\pi k\left(1 - \frac{h^2}{L^2}\right) = 2\pi k\left(1 + \frac{(h/R)^2}{4\pi^2}\right)^{-1}. \tag{2.12}$$

Combining (2.11) and (2.12), normalising by $2h^2/\Gamma$ and using $b^2 = h^2 - \Delta^2$, one obtains an expression for the dimensionless growth rate of the pairing instability in the helical geometry:

$$\sigma_p^*(k) = 2\pi k\left[1 - k\left(1 + \frac{(h/R)^2}{4\pi^2}\right)^{-1}\right]. \tag{2.13}$$

This result is plotted in figure 6(*a*) for the first lobe of the growth rate curve ($0 \leqslant k \leqslant 1$) (see figure 3), for three values of the non-dimensional pitch h/R. For $h \to 0$, the maximum growth rate is $\sigma_p^* = \pi/2$ for $k = 1/2$. For increasing pitch, the maximum growth rate increases, and it is reached at slightly higher wavenumbers. This is in very close agreement with the results from the full stability analysis of the helical geometry, an example of which is shown in figure 6(*b*).

The prediction of the growth rate in (2.13) is based on the assumption that the helical geometry can locally (in the azimuthal direction θ) be approximated by an

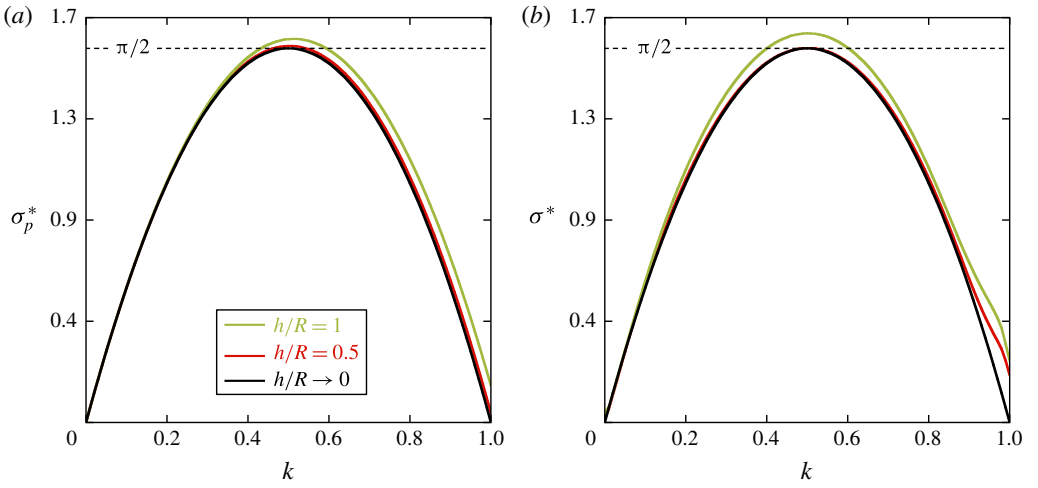

FIGURE 6. (Colour online) (*a*) Prediction of the growth rate for various h/R, based on the result (2.13) for two-dimensional pairing (Lamb 1932). (*b*) Growth rate from the full stability analysis of a helical vortex with $a_e/R = 0.1$ (Gupta & Loewy 1974).

array of straight vortices. The curvature of the vortex loops is neglected in this approach, as is the self-induced velocity due to this curvature. The core size a_e, which influences the curvature-induced velocity, does not appear in the analysis, which is based on a point vortex system. The dependence on this parameter in the full analysis is weak for thin-cored vortices ($a_e/R \lesssim 0.1$). Levy & Forsdyke (1927) have studied the stability of an infinite series of vortex rings, a configuration which, for small separation distances between the rings, resembles a helical vortex of small pitch. They also find a weak dependence of the growth rate on the curvature and core size in this parameter range, and as h/R (the normalised curvature) tends to zero, the non-dimensional maximum rate converges to the value $\pi/2$ for two-dimensional pairing.

The result in (2.13) is expected to become invalid for large helix pitch, for which the mutual interaction between neighbouring loops becomes much weaker and the dynamics are dominated by the local induction from the vortex curvature and torsion.

The present analysis can in principle be extended to wavenumbers k larger than 1. Since the phase difference Φ in the growth rate (2.11) for point vortex arrays is to be taken modulo 2π, the lobe of the growth rate curve in figure 6(*a*) repeats itself in the same way for higher k. However, as k increases, i.e. as the wavelength of the displacement perturbation decreases, the assumption of arrays of locally straight vortices becomes increasingly less valid. Robinson & Saffman (1982) have investigated the pairing instability for arrays of sinusoidally perturbed vortices. They found that the maximum growth rate decreases with increasing perturbation wavenumber, which is consistent with the decrease of the local maxima for the higher wavenumbers observed in figures 3 and 23.

It can be concluded that the growth rate of the long-wave displacement instability of a helical vortex with moderate pitch ($h \lesssim R$) and small core size ($a_e/R \lesssim 0.1$) is predicted remarkably well using the results from the classical pairing (in two or three dimensions) of infinite vortex arrays, showing that vortex pairing is the dominant mechanism involved in this phenomenon.

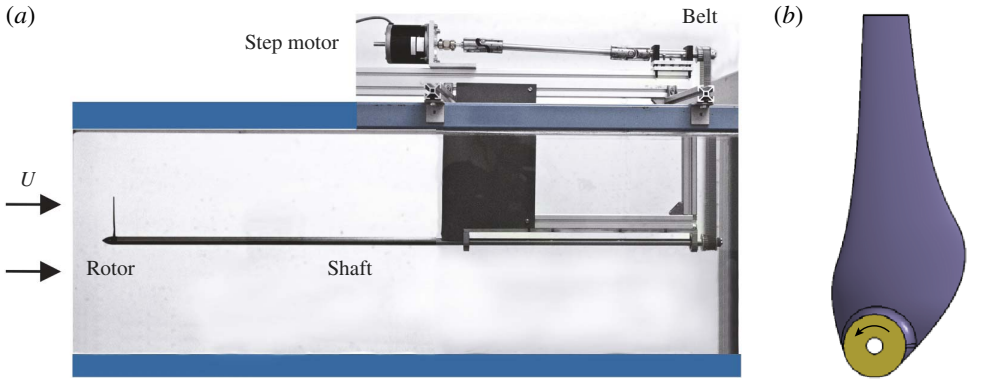

FIGURE 7. (Colour online) (*a*) Experimental set-up (side view of the water channel test section) and (*b*) schematic of the rotor blade geometry.

In the following sections, we describe an experimental study aimed at clearly identifying the pairing instability of a helical vortex in a real flow (wake of a rotor), and to compare measurements of its growth rate with theoretical predictions. Observations of the later stages of this phenomenon, not accessible by linear theory, are also shown.

3. Experimental details

3.1. *Set-up*

Experiments were carried out in a recirculating free surface water channel with a test section of dimensions 38 cm (height) × 50 cm (width) × 150 cm (length). A helical vortex was generated near the test section entry by a single-bladed rotor mounted on an ogive-tipped shaft (diameter 15 mm) and driven by a computer-controlled stepper motor outside the channel using a belt (figure 7*a*). The rotor blade geometry, shown schematically in figure 7(*b*), is based on the low Reynolds number airfoil A18 by Selig *et al.* (1995). It is designed to operate in the wind turbine regime and produce a constant radial circulation distribution (Joukowsky rotor) over the outer 75 % of the span, in order to generate a highly concentrated tip vortex. The chord and twist distributions of the blade are given in figure 8. The rotor has a radius $R_0 = 80$ mm and a tip chord $c_{tip} = 10$ mm. Details of the design procedure can be found in Bolnot (2012). For the present experiments, the blade is rotated at a frequency $f_0 = 6$ Hz, and placed in a uniform incoming flow of velocity $U = 36\ \mathrm{cm\,s^{-1}}$. This results in a tip chord-based Reynolds number of approximately 30 000 and a tip speed ratio $2\pi f_0 R_0/U = 8.4$, representing the design conditions for the blade geometry. Experiments were also carried out for two higher tip speed ratios (9.6 and 12.3), by varying the free stream velocity U, leading to lower values of the (non-dimensional) pitch. The results are qualitatively similar to the ones of the design case presented in the following sections, leading to the same overall conclusions.

3.2. *Perturbation method*

Although the helical vortex generated with this set-up is known to be unstable from theory, the turbulence intensity in the channel (<1 %) and the level of vibrations of the rotor support were low enough so that no significant perturbation of the helix shape

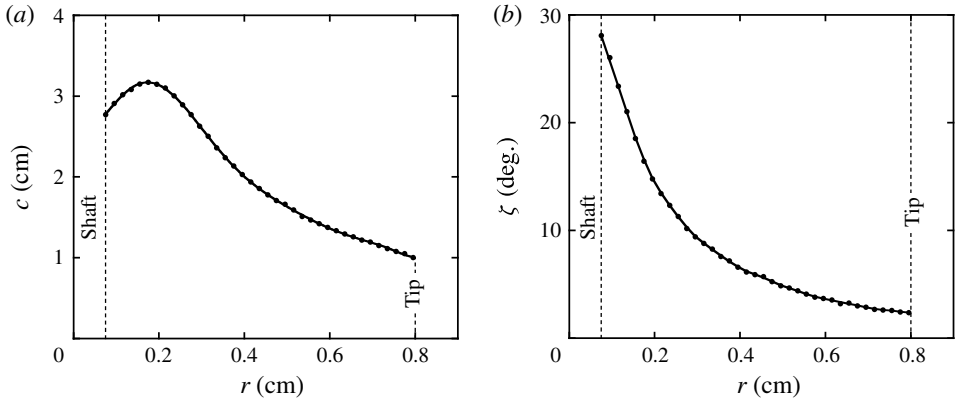

FIGURE 8. Radial distributions of (a) chord c and (b) twist angle ζ of the blade.

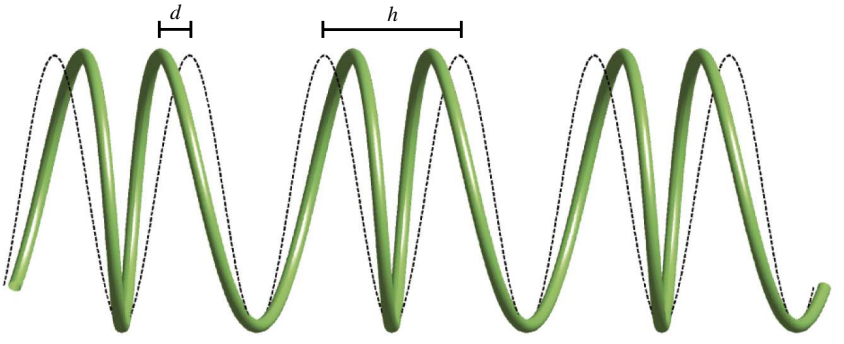

FIGURE 9. (Colour online) Schematic of the experimental helix perturbation consisting of an axial displacement ($k = 1/2$, $d/h = 0.2$). The dashed line represents the unperturbed geometry. The amplitude is chosen here to be much higher than in the experiments for improved visual clarity.

was visible in the field of observation, which covered approximately 10 turns (see figure 11). This made it possible to impose controlled displacement perturbations of the helix, by introducing suitable periodic modulations of the initially constant blade rotation frequency. Varying the rotation speed results in a shift of the tip vortex in the axial direction with respect to its unperturbed position. Based on the form of the unstable modes of the instability given by (2.8), we aim for a helix with a perturbed z-coordinate given by

$$z_p = \frac{h}{2\pi}\theta + d\cos(k\theta), \tag{3.1}$$

where d is the amplitude of the displacement. An example with an out-of-phase displacement of successive helix turns ($k = 1/2$) is shown schematically in figure 9. Given that, in the frame of reference of the helical vortex, the rotor moves with a velocity hf_0 in the axial direction, we may write $z = hf_0 t$. Derivation with respect to time and the relation $\dot{\theta} = 2\pi f$ then lead to

$$f = f_0\left[1 - 2\pi k\frac{d}{h}\sin(k\theta)\right]^{-1}, \tag{3.2}$$

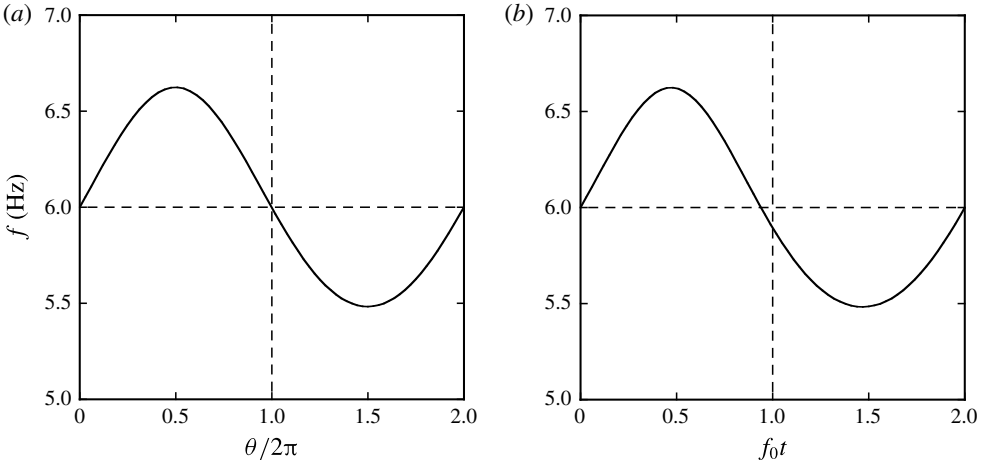

FIGURE 10. Modulation of the rotor rotation rate for a perturbation with $k = 1/2$ and $d/h = 0.03$: (a) as function of the angular position θ, and (b) as function of time t.

which gives the rotation rate of the rotor as function of its angular position. Numerical integration of (3.2) then provides the rotation rate as function of time, which is programmed into the step motor controller. Figure 10 contains an example of such a modulation, for the case shown in figure 9, with a typical value of the amplitude used in the experiments. The modulation has a period of 2 ($=1/k$) rotor cycles. The rotation is faster than the mean in the first cycle and slower in the second. Whereas the rate varies almost sinusoidally with the azimuthal position (for small d/h), the dependence on time is more distorted. The motor (Parker CompuMotor AMP 5034-232) and controller (Parker Gemini GT6K) have a maximum resolution of 128 000 microsteps per revolution, which enables them to execute the prescribed modulation precisely. Amplitudes of only a few per cent of the helix pitch were sufficient to trigger the desired instability mode.

The amplitude of the frequency modulation in figure 10 corresponds to about 10 % of its mean value. Surprisingly, this rather large variation does not induce a modulation of the vortex parameters of the same order, as might have been expected. It was found from particle image velocimetry (PIV) measurements that the circulation and core sizes vary by only a few per cent during a typical perturbation cycle, as long as the deformation amplitude d/h remains below 5 %. This variation lies within the uncertainty intervals for these parameters in the measurements of the unperturbed flow presented in § 4 below. We therefore conclude that the perturbation method does not significantly modify the helical base flow properties.

3.3. *Visualisations and measurements*

The helical vortex structure was visualised using fluorescent dye (Leweke 2012). The rotor set-up could be tilted to be able to apply the fluorescent paint (thickened fluorescein solution) to the blade tip outside the water. When the spinning rotor was lowered into channel test section with the water flowing, the dye was washed off and clearly marked the tip vortex. Volume illumination was achieved with light from an argon ion laser (model Stabilite 2017 by Spectra Physics), coupled to an optical fibre equipped with a spherical lens. The helical wake established itself after a short

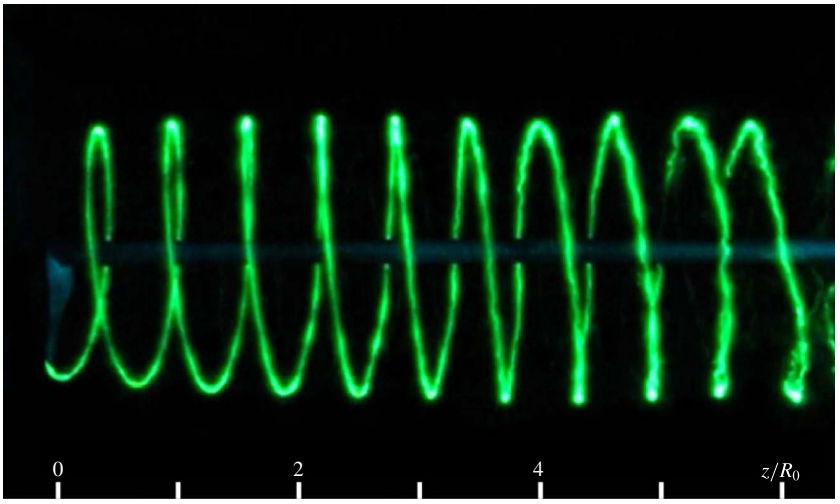

FIGURE 11. (Colour online) Dye visualisation of the unperturbed helix. The rotor is on the left, flow is from left to right. The vertical shaft support is located on the right, just outside the field of view.

transient, and observation was possible for about 30 s (180 blade rotations) before the dye disappeared. Images and video sequences were recorded with a standard digital camera (Canon IXUS 220 HS) in high-speed mode at 120 images per second. These visualisations were also used to obtain quantitative information about the vortex geometry (radius, pitch) and to measure the instability growth rates, as explained in § 5.2. Additional visualisations were obtained by injecting a dye solution at a fixed location in the rotor plane in order to observe and measure the flow along the vortex centre (see figure 16 below).

Velocity fields and vorticity distributions were obtained from PIV. A Nd-YAG pulsed laser (Quantel Twins Ultra 190) was positioned underneath the test section to generate a 3 mm vertical light sheet illuminating the centre plane of the rotor flow (only half of the plane was illuminated behind the rotor since the shaft blocked the light). The flow was seeded with 30 μm plastic particles, and images were recorded with a resolution of 2000 × 1336 pixels using a Roper Redlake digital camera. The images were processed using an in-house code based on an algorithm developed by Meunier & Leweke (2003), which has been successfully employed in previous experimental studies of vortex flows (see, e.g. Meunier & Leweke 2005; Roy *et al.* 2011). PIV measurements were used to determine the base flow properties of the helical rotor wake (circulation, core size, etc.).

Further details about the experimental set-up and procedures are given in Bolnot (2012).

4. Unperturbed rotor wake

We first present the flow generated in the wake of the one-bladed rotor without any perturbation, and determine the properties of the helical tip vortex serving as the base configuration for the stability study.

Figure 11 shows a dye visualisation of the unperturbed tip vortex. A regular helical shape is observed over a distance of three rotor diameters. Towards the end of

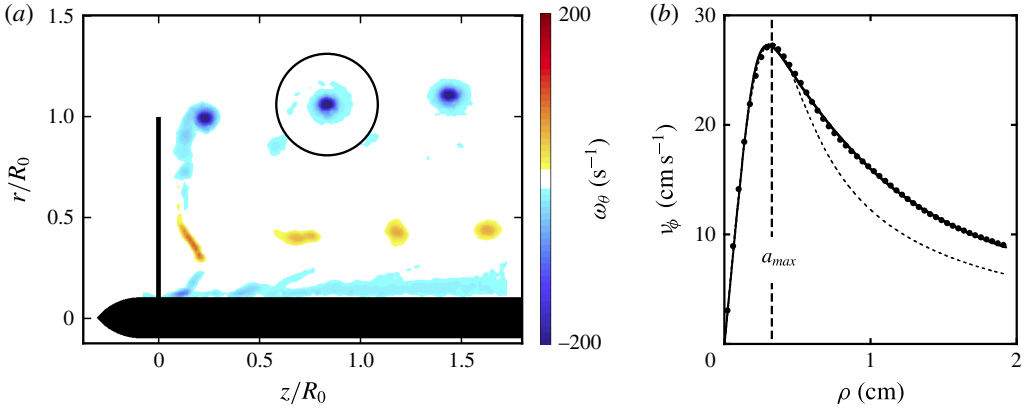

FIGURE 12. (Colour online) (*a*) Phase-averaged distribution of azimuthal vorticity ω_θ in the central plane of the rotor, obtained from 100 instantaneous PIV fields. (*b*) Mean velocity profile of the tip vortex inside the circle in (*a*); the measurements (●) are well fitted by the VM2 profile (—) of Fabre & Jacquin (2004). The dashed line is a fit to the profile of a Gaussian vortex with the same maximum.

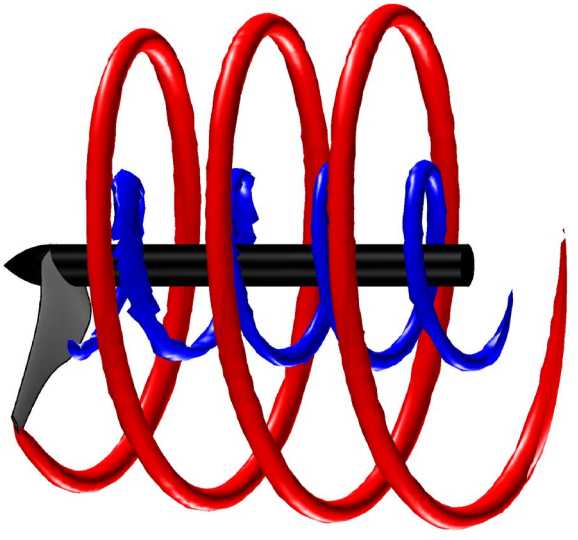

FIGURE 13. (Colour online) Three-dimensional reconstruction of the tip and root vortices, using 20 phase-averaged vorticity fields as in figure 12. Isosurfaces of the azimuthal vorticity are plotted for $\omega_\theta = 50$ s^{-1} (red) and $\omega_\theta = -20$ s^{-1} (blue).

the observation interval, some distortions of the vortex filament are seen, which are induced by the presence of the shaft's support structure (see figure 7*a*). The periodicity of the flow is illustrated by the superposition of instantaneous dye images, recorded at intervals of one rotor period, shown in figure 20. The unperturbed configuration in figure 11 is the reference case of our study. It is quite close to the theoretical base flow in figure 1, even if its geometry evolves slightly in the downstream direction, as shown by the measurements below.

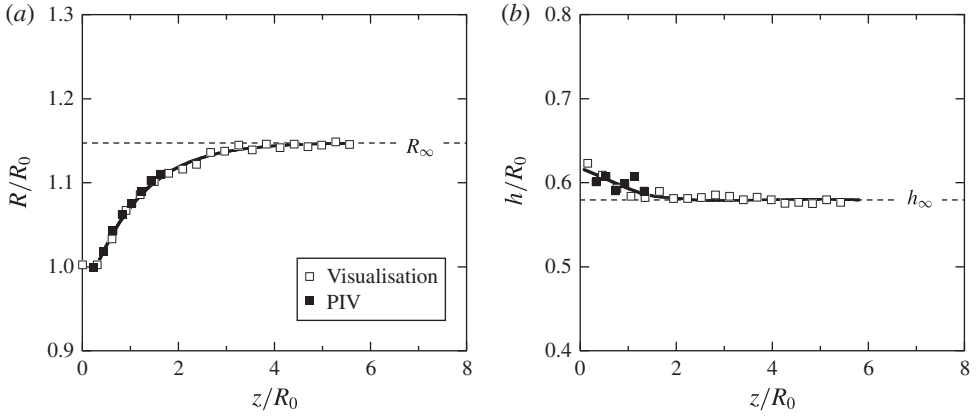

FIGURE 14. Downstream evolution of helix parameters. (*a*) Radius R; (*b*) pitch h.

The phase-averaged azimuthal vorticity field in the near-wake centre plane of the rotor, obtained from 100 instantaneous PIV fields, is presented in figure 12(*a*). The cross-sections of the tip vortex are clearly visible. One also recognises the signature of the blade's root vortex of opposite-signed vorticity at $r/R_0 \approx 0.4$, as well as the boundary layer on the shaft. A series of these fields, taken at different phases of the blade rotation, can be used to reconstruct the vortex structures in three dimensions, by interpolation in the azimuthal direction θ. The result in figure 13 shows that the inner root vortex, not visible in the dye visualisations, has a different pitch than the blade tip vortex.

The visualisations and PIV measurements were used to evaluate the geometrical parameters and the vortex properties of the base flow. The radius and pitch of the helical tip vortex were measured directly from the visualisations, by locating the centres of the dye loops at the top and bottom of the helix. Since some fluctuations were observed in the downstream part of the helix (see figure 20*a*), 5–7 individual images were treated for each measurement in order to determine the mean positions with precision. The helix radius and pitch are plotted as functions of the distance from the rotor in figure 14. The radius shows the typical downstream increase for the wake of a rotor in the wind turbine regime. It grows from its initial value R_0 by about 15 % and reaches its asymptotic value R_∞ two diameters behind the rotor. The pitch is found to be remarkably constant from the start. It is about 58 % of the blade span. R and h were also determined from PIV measurements, using the coordinates of the maxima of azimuthal vorticity; the agreement between the two sets of measurements is good. The pitch of the root vortex is about 75 % of the tip vortex pitch, i.e. about $0.5R_0$, which makes the pitch-to-radius ratio larger than 1 for this vortex.

The circulation of the tip vortex was calculated from the PIV velocity data using a line integral on a circular path centred on a given vorticity maximum (see figure 12*a*). The diameter of the path was $0.4R_0$, which allowed capturing all of the vorticity 'belonging' to one helix loop. The circulation calculated in this way, in figure 15(*a*), increases gradually over a distance of one rotor radius, which is reminiscent of the roll-up process of the initial vortex sheet shed by the blade. The value Γ_∞ measured at the downstream end of the PIV field is kept as the reference circulation. A recent comparison with numerical simulations of exactly the same configuration, reported in

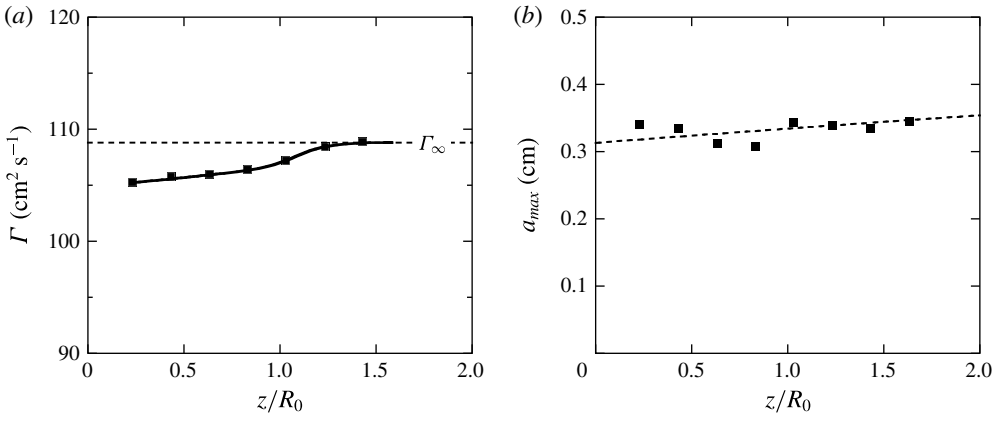

FIGURE 15. Vortex parameters, as determined from particle image velocity measurements. (*a*) Circulation Γ; (*b*) core size a_{max}. The dashed line in (*b*) represents a fit to the viscous evolution for a two-dimensional Gaussian vortex: $a_{max} = 1.12\sqrt{4\nu(t - t_0)}$.

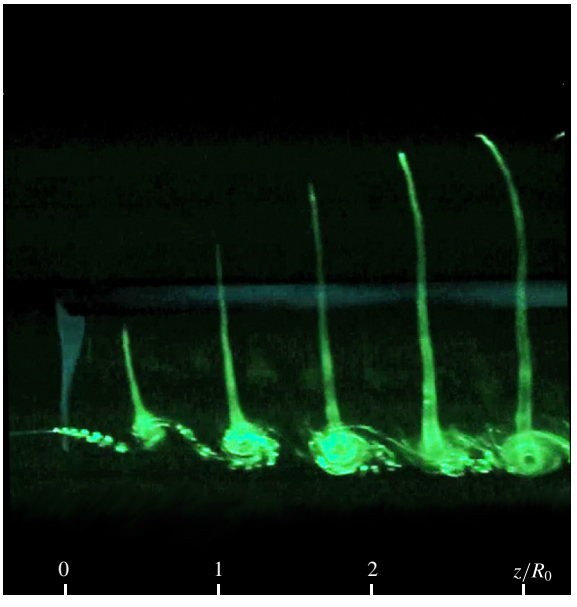

FIGURE 16. (Colour online) Visualization of the axial flow inside the core of the unperturbed helix. Dye is continuously injected at a fixed location in the rotor plane.

Ivanell *et al.* (2015), confirmed that the circulation does not vary by more than 1 % further downstream. The root vortex circulation was obtained with a similar procedure, its value is about 30 % of the tip vortex circulation.

The velocity profile of the vortex was obtained by considering the local polar coordinates (ρ, ϕ) inside the circle mentioned above (see also figure 2). A profile of the azimuthally-averaged azimuthal velocity in these coordinates, from which the core size a_{max} can be determined, is presented in figure 12(*b*) (the angle between the vortex axis and the θ-direction is small enough, around 5°, to be ignored). The downstream

evolution of a_{max} in figure 15(*b*) shows some scatter, but it roughly follows the viscous growth of a Gaussian vortex. Since the helix radius increases downstream, the tip vortex is subject to stretching along is centreline, which in turn acts against the viscous growth of the core radius. One can estimate that the combination of these two effects results in a variation of the core size of about 15 % over the interval where the linear instability is typically observed. A representative value near $z/R_0 = 2$ is taken as reference. The velocity profile in figure 12(*b*) is not very well represented by that of a Gaussian vortex. If the core region ($\rho \lesssim a_{max}$) is fitted to such a profile (dashed line in figure 12*b*), the velocities are underestimated further from the centre, which indicates that the outer region also contains some amount of circulation. A vortex model incorporating this feature is the smooth two-scale profile proposed by Fabre & Jacquin (2004), named VM2 in their paper, which is indeed found to fit the experimental data much better. One may ask what influence this difference has on the long-wave instability, and in particular on its growth rate. The core size and velocity profile determine the self-induced velocity of the vortex (see § 2.1). Fabre (2002) has calculated the dispersion relations for perturbations (Kelvin modes) of both types of vortices, Gaussian and VM2. One of these modes, a displacement mode of azimuthal (ϕ) wavenumber 1, can be related to the self-induced velocity of a curved vortex. The results of Fabre (2002) show that the corresponding dispersion relation, when scaled using Γ and a_{max}, is almost identical for both types of vortices, in particular in the range of small wavenumbers we are concerned with here ($k_l a_{max} \lesssim 0.5$). This means that, if a_{max} is the same, both profiles have a very similar equivalent core size a_e, and that we can use the procedure for Gaussian vortices described in § 2.1 also for our case.

The tip vortex generated in the present experiment was also found to contain a velocity component along its axis, which takes the form of a core jet in the ξ-direction (figure 2). This jet can be visualised by using the following technique: instead of coating the blade tip with dye, a thin tube is used to continuously inject dyed fluid at a fixed location in the rotor plane ($z = 0$), close to the point where the blade tip passes, at $r = R_0$. Figure 16 shows that the dye is transported away from this location within the core of the tip vortex, following the motion of the blade. In the reference frame moving with the blade, this represents a velocity deficit inside the tip vortex core, which is likely to be caused by losses in the boundary layers. The shape of the dye pattern directly represents the axial velocity profile. We assume here that it can be approximated by an axisymmetric Gaussian profile, as given by (2.2). One can measure the maximum velocity V_ξ^{max} (speed of the dye tip) and characteristic radial scale (half-width at a fraction $1/e$ of the profile height) of such a profile from these visualisations. The latter is close to the core size a determined from the azimuthal velocity profile. The maximum axial velocity is of the same order as the maximum swirl velocity, or about 10 % of the blade tip speed. The measurement from the dye pattern results in an uncertainty of around 7 % (more precise 3-component PIV measurements were not carried out), which is nevertheless acceptable for the calculation of the equivalent core size (2.7).

Table 1 summarises the measured geometrical and vortex properties for the rotor wake base flow, and the resulting non-dimensional parameters characterising the helical tip vortex. The stated uncertainties result from the scatter of individual measurements, as well as from estimates of the reliability of the employed procedures. The values for h_∞/R_∞ and a_e/R_∞ are used for the theoretical prediction of the growth rate of the pairing instability in our rotor wake.

Γ_∞	$= (109 \pm 2)$ cm^2 s^{-1}	Re	$= 10\,900\ (\pm 200)$
V_ξ^{max}	$= (30 \pm 2)$ cm s^{-1}	W	$= 0.54\ (\pm 0.08)$
R_∞	$= (9.2 \pm 0.1)$ cm		
h_∞	$= (4.6 \pm 0.1)$ cm	h_∞/R_∞	$= 0.50\ (\pm 0.01)$
a_{max}	$= (0.35 \pm 0.04)$ cm	a_e/R_∞	$= 0.053\ (\pm 0.008)$

TABLE 1. Measured parameters of the unperturbed helical tip vortex.

5. Instability of the helical vortex

5.1. *Unstable modes*

As seen in figure 11, the helical vortex generated by the blade spinning at a constant rate does not show any significant deformation over the first 3–4 diameters behind the rotor, even if some 'scatter' occurs towards the end of this interval (figure 20*a*), likely caused by some interference with the rotor support structure located just outside the field of view. As soon as the flow is perturbed through a modulation of the blade rotation, as explained in § 3.2, deformations of the initially regular helix become visible a short distance behind the rotor, and they are rapidly amplified as the vortex moves downstream, showing that the vortex is indeed unstable with respect to these perturbations. Figures 17 and 18 contain dye visualisations of a number of different perturbation modes, for various azimuthal (θ) wave numbers k, along with the theoretical counterparts from the stability analysis.

The modes in figure 17 correspond to the first four maxima of the growth rate curve (figures 3 and 23), for which k is an odd multiple of $1/2$. For these cases, the perturbation repeats itself after two blade revolutions, and the displacements of neighbouring helix loops are exactly out of phase. Local pairing occurs at azimuthal locations where the displacement is maximal. The phase of the blade rotation modulation was chosen so that pairing always occurs at the top. For $k = 1/2$, this is the only location of pairing; for the higher wavenumbers, additional locations around the azimuth of the helix can be identified. The pattern for $k = 3/2$ in figure 17(*b*) is the same as found by Walther *et al.* (2007) in their figure 9. The theory in § 2.2 predicts a spatially uniform temporal growth in an infinite helical vortex. In the experimental configuration, the vortex is generated continuously by the rotor blade, and perturbations grow (in time) as they are convected downstream. In the frame of reference of the rotor, this results in a spatial growth of the perturbation amplitude. The amplitude at a given downstream position depends on its initial value, as well as on the growth rate of the mode. For the examples shown in figures 17 and 18, forcing amplitudes d/h_∞ (see (3.2)) between 3 % and 5 % were used. The dependence of the wake evolution on this parameter is further discussed in § 6.

Perturbation amplitudes of the same order as for the theoretical shape on the right-hand side of figure 17 are found near the centre of the experimental visualisation on the left. The observed deformations are extremely close to the theoretical predictions for an infinite helix. This demonstrates that we are indeed observing a convective long-wave (pairing) instability in our flow, and it also shows that the the pairing mechanism depends mainly on the immediate vicinity of a given vortex group.

Figure 18 presents further instability modes, with wavenumbers below the first maximum of the growth rate curve. These perturbations are more complex than the ones of figure 17, their shapes repeat after a larger number of cycles. Their amplitudes

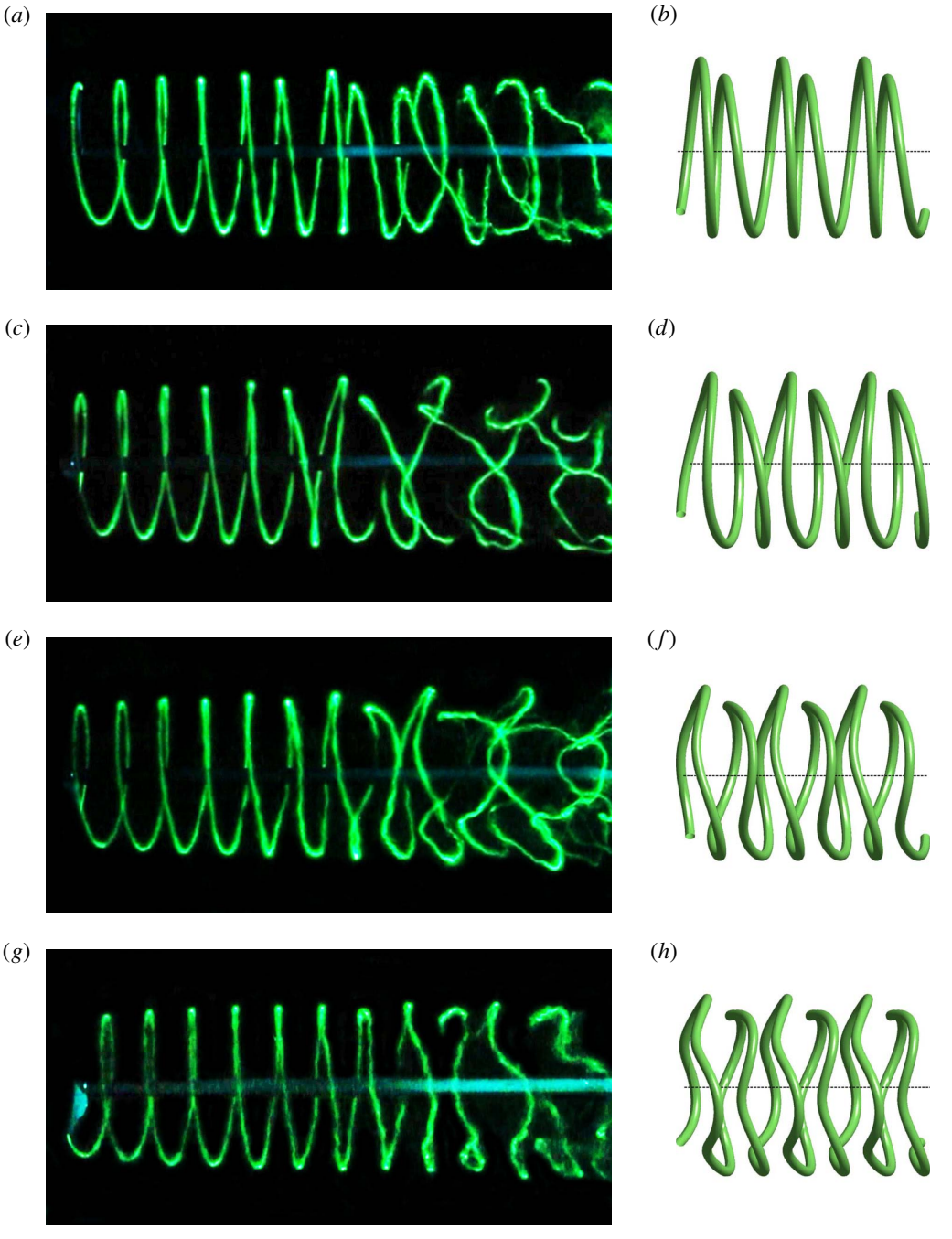

FIGURE 17. (Colour online) Most unstable perturbation modes. (*a*,*c*,*e*,*g*) Experimental dye visualisations; (*b*,*d*,*f*,*h*): sketches of the theoretical mode shapes. (*a*,*b*) $k = 1/2$; (*c*,*d*) $k = 3/2$; (*e*,*f*) $k = 5/2$; (*g*,*h*) $k = 7/2$.

nevertheless grow downstream, showing their unstable nature. Again, a close similarity between experimentally observed and theoretically predicted deformation shapes is found.

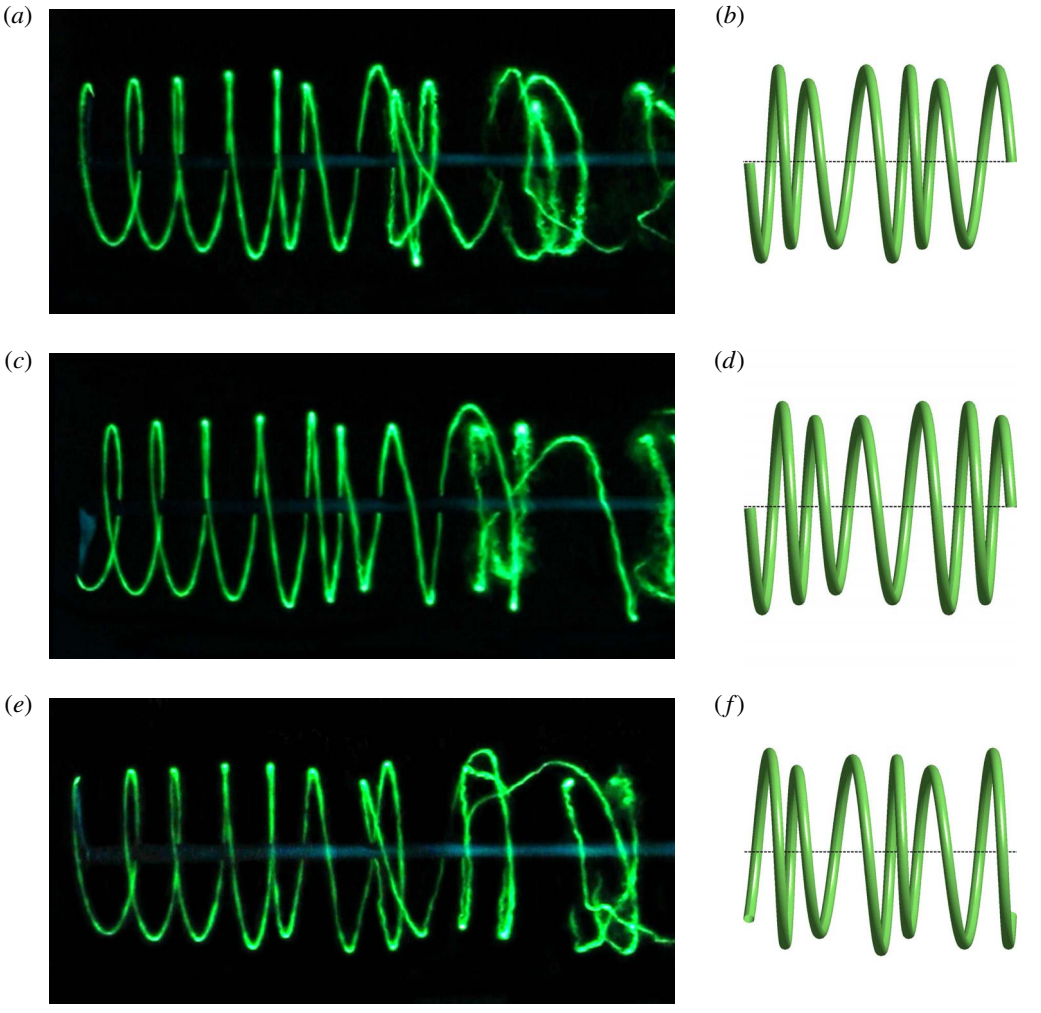

FIGURE 18. (Colour online) Subharmonic instability modes. (*a*,*c*,*e*) Experiment; (*b*,*d*,*f*) theory. (*a*,*b*) $k = 1/3$; (*c*,*d*) $k = 1/4$; (*e*,*f*) $k = 2/5$. The deformation pattern repeats after 3, 4 and 5 helix/rotor turns, respectively.

Finally, figure 19 shows a case where the tip vortex is perturbed with a wavenumber $k = 1$. For integer values of k, theory predicts a growth rate close to zero. Indeed, the perturbed flow in figure 19 is practically indistinguishable from the base flow in figure 11: the imposed perturbations are only very weakly amplified.

Overall, our experiments show that the rotor wake is highly receptive to a large variety of deformation perturbations corresponding to the modes of the theoretically predicted long-wave instability of a helical vortex.

5.2. *Growth rates*

It was possible to determine the growth rates of the various deformation modes seen in the previous section from video sequences of the helical vortex visualised with dye. For each case, the sequence started with a phase of unperturbed flow, serving as the

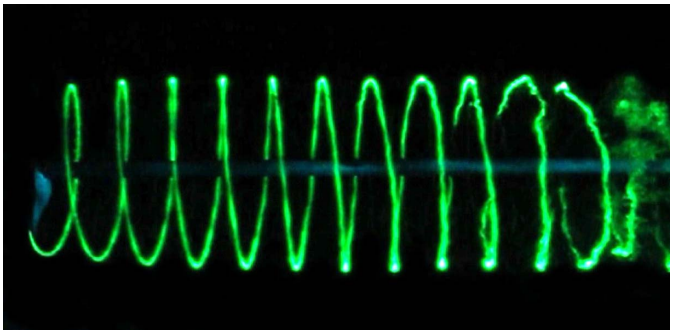

FIGURE 19. (Colour online) Helical vortex perturbed with $k = 1$ and $d/h_\infty = 0.03$. The displacement is in phase between successive helix turns. No amplification of the perturbation can be detected.

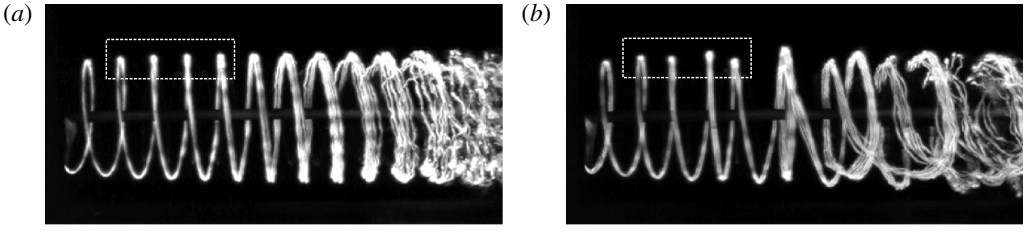

FIGURE 20. Superposition of 10 instantaneous dye images recorded at the same phase of the blade motion. (*a*) Unperturbed flow; (*b*) perturbed flow with $k = 1/2$ and $d/h_\infty = 0.03$. The white rectangles show the regions represented in figure 21.

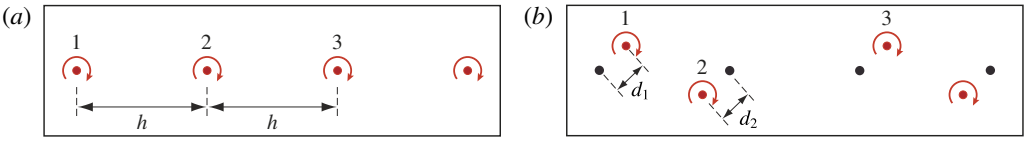

FIGURE 21. (Colour online) Schematic illustrating the determination of the base flow and perturbation properties from dye visualization. (*a*) Unperturbed and (*b*) perturbed helix. The dots represent the vortex centre positions in the upper part of the centre plane.

reference configuration, before the rotation modulation was switched on. In figure 20, several images with the same rotor position are superposed for each of the two phases of one such recording. The mean positions of the upper sections of the vortex loops were then detected for the unperturbed and perturbed flows, and the distance between them (d_1 and d_2 in figure 21) calculated as function of the downstream position. The evolution of this distance with time can be directly deduced from the rotor mean frequency f_0 and the frame rate of the camera. Measurements of the amplitude were made up to the point where two successive helix loops first swap their axial position z (near the centre of the images in figure 20). Up to this point, the patterns are very repeatable, so that five images were sufficient to obtain the average positions with precision for each case.

Figure 22 shows a typical growth of the perturbation amplitude as function of time. At $t = 0$ the tip vortex leaves the rotor plane. After an initial transient phase,

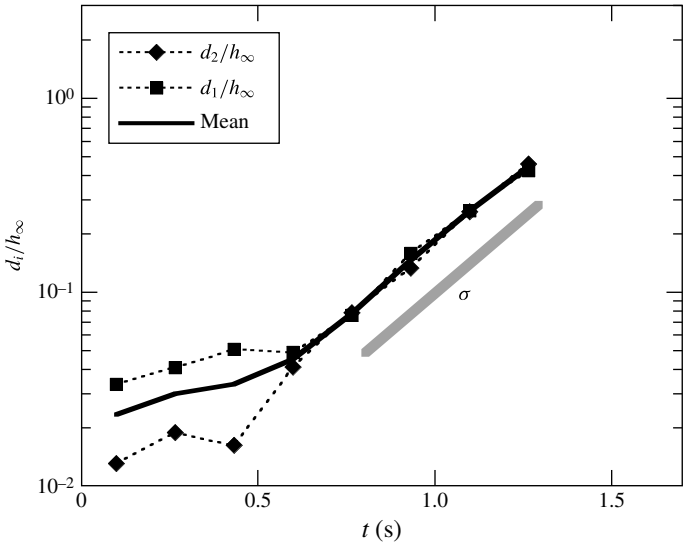

FIGURE 22. Growth of the displacement amplitudes d_i for a perturbation with $k = 3/2$ and $d/h_\infty = 0.03$. The slope of the linear part represents the growth rate σ.

in which the deformation adjusts from the imposed axial displacement to the proper eigenmode of the instability, the amplitude increases exponentially for about 0.7 s, which corresponds to a distance of about $4h_\infty$ or $2R_0$. The end of this exponential growth corresponds roughly to the time/location where the loop swapping occurs, with a displacement amplitude close to $0.5h_\infty$. The growth rate is found by fitting an exponential function to the measured data.

The above procedure was repeated for 11 different wavenumbers, including all examples shown in the previous section. The resulting growth rates are plotted in figure 23, non-dimensionalised by the measured helix properties. Figure 23 also contains the theoretical prediction for the pairing instability of an infinite helical vortex, using the parameter values listed in table 1. The agreement between experiment and theory is very good. In the theoretical analysis of § 2.2, the presence of an inner blade root vortex is not taken into account. Adding a straight vortex of the same circulation as the tip vortex (but of opposite sign) on the helix centre line in the calculations, results in a variation of the instability growth rate of only a few per cent. The root vortex in our experiments (figures 12*a* and 13) is much weaker than the tip vortex, probably due to the presence of the shaft. Its effect on the growth rate therefore lies well within the uncertainty interval of the measurements and was therefore not considered in the theory.

6. Nonlinear evolution

The previous section has shown that, in the near wake of the rotor, the deformations of the (perturbed) blade tip vortex have the spatial structure of the unstable modes from the linear stability analysis of the flow. This structure persists, with an exponentially growing amplitude, until the local pairing of the helix loops leads to an exchange of the axial positions (swapping) of two neighbouring vortices that have been grouping together through the pairing instability. From this point onwards, the vortex loses its linear mode geometry and becomes highly distorted. This can

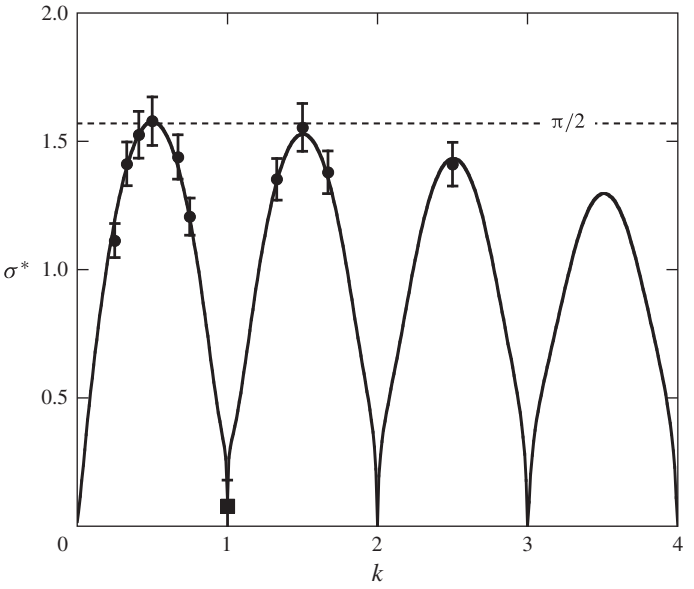

FIGURE 23. Growth rates of the long-wave instability. The symbols represent experimental measurements, and the line the corresponding theoretical prediction from Gupta & Loewy (1974) using the values in table 1.

be partly seen in figures 17 and 18. Despite the complicated interlaced shape of the vortex loops, the filament structure appears to remain intact up until the downstream end of the observation interval. No cross-linking or breakdown to small-scale turbulent motion is observed, which is probably related to the very small core diameter of the tip vortex. The superposition of images in figure 20(*b*) shows that, despite some scatter, the flow is still remarkably periodic.

In order to explore this evolution to even later stages, experiments were carried out with higher forcing amplitudes, up to $d/h = 0.15$. This created a higher initial displacement of the vortex, and therefore a shorter downstream length of the linear range, leaving more observation distance for the subsequent nonlinear regime. Figure 24 shows a series of rotor wake visualisations, where the most unstable perturbation (with $k = 1/2$) is triggered with different initial amplitudes. As this amplitude increases, the swapping location (marked by an arrow, and subsequently called z_s) moves upstream towards the rotor, as expected. The vortex remains intact well beyond the end of the linear regime. Only for the highest forcing amplitude a disintegration of the filament into small-scale structures is observed, beyond about twice the swapping distance. For this case, the large variations of the blade rotation rate result in non-uniform vortex properties along the filament, which may partly be responsible for the breakdown.

Inspired by the work of Felli *et al.* (2011) on propeller wakes, we computed the time-averaged dye patterns, over a period of 16 rotor cycles, from visualisation sequences of the cases shown in figure 24. The result in figure 25 reveals a fairly uniform mean structure of the wake, but the swapping location appears clearly as the minimum of a partial local contraction of the dye pattern. The dependence of the measured swapping distance z_s, obtained from the images in figure 25 and two further intermediate cases, is shown in figure 26. z_s is found to decrease by more than 60 %

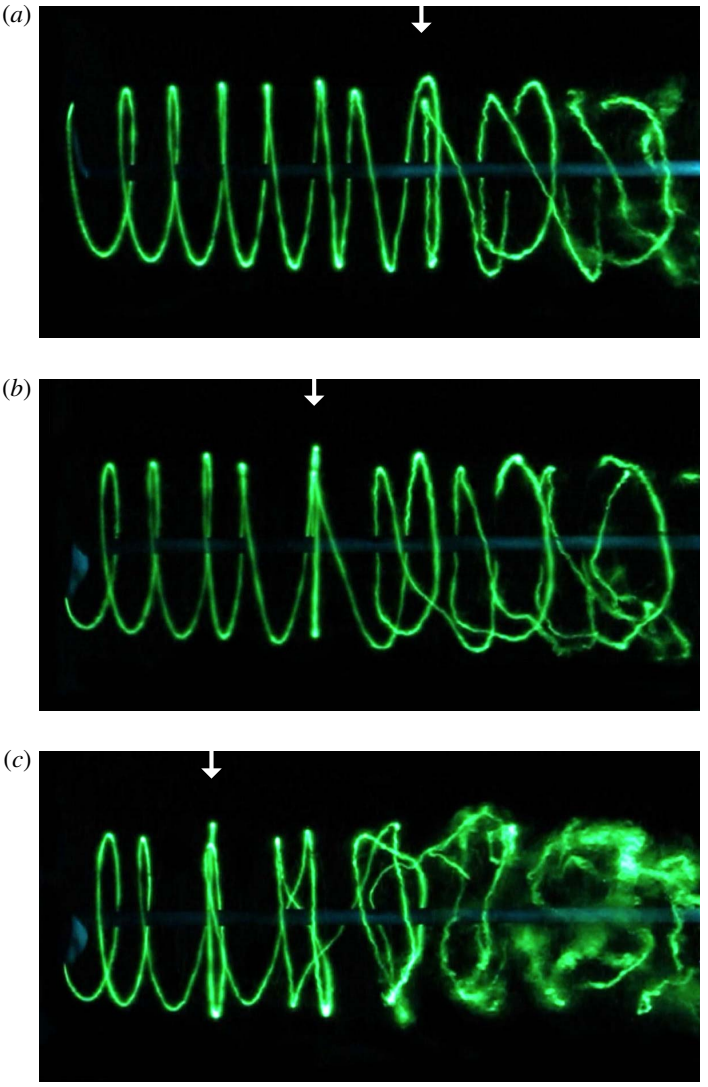

FIGURE 24. (Colour online) Rotor tip vortex evolution as function of initial perturbation amplitude for the most unstable mode with $k = 1/2$. (*a*) $d/h = 0.01$; (*b*) $d/h = 0.05$; (*c*) $d/h = 0.15$. The arrows show the locations where two successive helix loops first swap places.

as the initial displacement amplitude is increased from $d/h = 0.01$ to $d/h = 0.15$. Assuming that the rotor wake evolution is governed by the convective exponential growth of the pairing instability, and that the swapping of helix loops occurs for a certain constant value of the perturbation amplitude, one can derive an expression for the swapping location of the form

$$z_s/R_0 = c_1 - c_2 \ln(d/h), \tag{6.1}$$

where c_1 and c_2 are constants depending on the flow and instability properties. The values of these constants were found for the data in figure 26 by a least-squares fit,

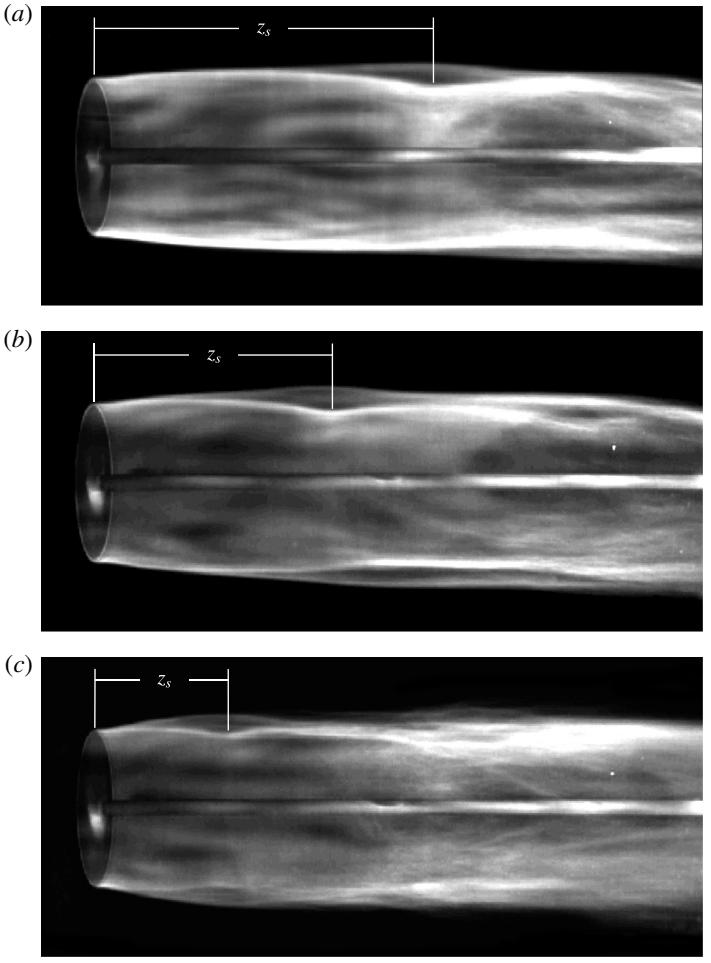

FIGURE 25. Time-averaged dye patterns for the perturbed (with $k = 1/2$) helical rotor wakes shown in figure 24, allowing the determination of a characteristic distance z_s for the downstream evolution. (*a*) $d/h = 0.01$; (*b*) $d/h = 0.05$; (*c*) $d/h = 0.15$.

and the result is in good agreement with the measurements. Sørensen *et al.* (2014) have carried out a similar analysis concerning the downstream evolution of the pairing instability in their numerical study of the wake of a three-bladed wind turbine. They have established a link between the constants in (6.1) and the rotor properties (number of blades, tip speed ratio, thrust coefficient) and instability growth rate, as well as between the initial perturbation amplitude and the turbulence intensity of the incoming flow, acting as the trigger for the instability in their case.

7. Summary and conclusion

In this paper, we have explored the long-wave instability of a single helical vortex, which is one of the elementary structures in vortex dynamics, and which is used to model the wake generated by rotating lifting surfaces (rotors) in various configurations. As shown in earlier stability analyses (Widnall 1972; Gupta & Loewy 1974), which were partly corrected and extended here, the long-wave instability

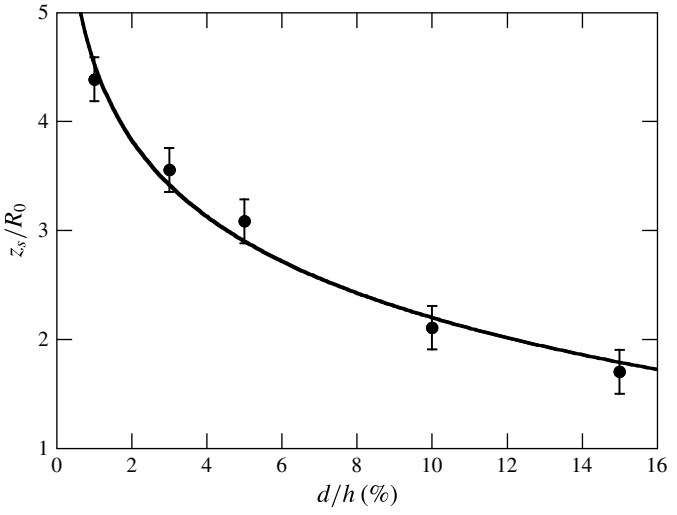

FIGURE 26. Characteristic distance z_s of wake evolution as function of the initial perturbation amplitude d. The line represents (6.1), with $c_1 = -0.1$ and $c_2 = 1.0$.

involves the amplification of displacement perturbations deforming the initial helix without modifying the core structure of the filament. A closer look at the spatial structure of the unstable modes reveals that, for small helix pitch ($h/R \lesssim 1$), for which the dynamics are dominated by the mutual interaction between helix turns, these deformations can be explained by a vortex pairing mechanism between neighbouring loops of the vortex. The most unstable deformations are out of phase between successive loops. A correspondence was established between the classical two-dimensional pairing of a periodic array of identical straight vortices and the helix instability, which allowed an accurate prediction of the instability growth rate from the results for two-dimensional pairing, in the regime of small pitch and small core size ($a/R \lesssim 0.1$).

An experimental study was carried out, where a helical tip vortex is generated by a one-bladed rotor in a water channel. An accurate perturbation method involving a modulation of the blade rotation, combined with a low level of noise in the flow, made it possible for the first time to observe and characterise the various unstable modes one by one. Detailed comparisons between experimental and theoretical results were made concerning the geometry of the deformed helix and the growth rate of the perturbations. The very good agreement between the temporal stability analysis of a spatially uniform infinite helix and the results obtained for the spatially evolving experimental flow show that the dynamics of a given vortex loop only depends on a few nearest neighbours. It shows that the long-wave instability in the wake of a rotor is indeed a convective process, and that one can deduce the spatial evolution from the temporal one via the vortex convection speed.

In our experiments, the helical tip vortex was found to be extremely receptive to even the slightest perturbations. Initial displacements as low as 1 % of the helix pitch were sufficient to lock the rotor wake in a particular unstable mode, leading to an entirely different wake evolution (figure 24*a*) than for the unperturbed case (figure 11). Vortex pairing has been observed in a number of previous experimental studies involving rotor wakes (Alfredsson & Dahlberg 1979; Stack *et al.* 2005; Felli

et al. 2011; Ohanian *et al.* 2012; Sherry *et al.* 2013; Naumov *et al.* 2014; Nemes *et al.* 2015). In all of these experiments, the rotors had at least two blades, and in most cases it is not clear to which degree the rotor geometry is really symmetric. Given the high receptivity of the helical vortices to initial perturbations, even a very small asymmetry in the set-up, which is often unavoidable, may have led to the observed pairing behaviour in these flows. The use of a one-bladed rotor in the present study avoids this problem, allowing a controlled selection of the perturbation.

The experimental observations shown in this paper can all be related to the stability of an idealised infinite helical vortex, as determined by Widnall (1972), Gupta & Loewy (1974). A further step in the theoretical analysis would be to consider the spatio-temporal dynamics of the pairing instability of a helical vortex, similarly to the work of Bolnot *et al.* (2014) for an array of vortex rings, since the presence of the rotor selects a particular (moving) reference frame for the helix. In addition, the variation of the helix parameters in the downstream direction (e.g. in figure 14*a* for the radius R) could be taken into account in a global stability analysis of the semi-infinite helical vortex. These extensions could, for example, help establish a link between the long-wave pairing instability treated in the present work and the more violent transition of a rotor wake to a vortex ring state (Leishman *et al.* 2004) known from helicopter aerodynamics. Helical vortex wakes in full-scale applications often have a similar geometry (h/R), but smaller relative core size (a/R) and significantly larger Reynolds numbers ($\sim 10^6$). The pairing instability will also occur in these conditions, in a similar manner to that described in this paper, although additional effects, such as atmospheric turbulence, may lead to more complex evolution scenarios.

Acknowledgements

The authors are grateful to Robert Mikkelsen and Jens Sørensen from DTU Wind Energy (Copenhagen) for their valuable advice on rotor design. This work was supported by the French Agence Nationale de la Recherche through the A*MIDEX grant (ANR-11-IDEX-0001-02), project LABEX MEC (ANR-11-LABX-0092) and project HELIX (ANR-12-BS09-0023-01).

REFERENCES

ALFREDSSON, P. H. & DAHLBERG, J. A. 1979. A preliminary wind tunnel study of windmill wake dispersion in various flow conditions, *Technical Note* AU-1499, FFA, Stockholm, Sweden.

ASH, R. L. & KHORRAMI, M. R. 1995 Vortex stability. In *Fluid Vortices* (ed. S. I. Green), pp. 317–372. Kluwer.

BETCHOV, R. 1965 On the curvature and torsion of a vortex filament. *J. Fluid Mech.* **22**, 471–479.

BHAGWAT, M. J. & LEISHMAN, J. G. 2000 Stability analysis of helicopter rotor wakes in axial flight. *J. Am. Helicopter Soc.* **45**, 165–178.

BOLNOT, H. 2012. Instabilités des tourbillons hélicoïdaux: application au sillage des rotors. PhD thesis, Aix-Marseille Université, Marseille, France.

BOLNOT, H., LE DIZÈS, S. & LEWEKE, T. 2014 Spatio-temporal development of the pairing instability in an infinite array of vortex rings. *Fluid Dyn. Res.* **46**, 061405.

CROW, S. C. 1971 Stability theory of a pair of trailing vortices. *AIAA J.* **8**, 2172–2179.

FABRE, D. 2002. Instabilités et instationarités dans les tourbillons: application au sillages des avions. PhD thesis, Université Pierre et Marie Curie–Paris VI, Paris, France.

FABRE, D. & JACQUIN, L. 2004 Short-wave cooperative instabilities in representative aircraft vortices. *Phys. Fluids* **16**, 1366–1378.

FELLI, M., CAMUSSI, R. & FELICE, F. D. 2011 Mechanisms of evolution of the propeller wake in the transition and far fields. *J. Fluid Mech.* **682**, 5–53.

FUKUMOTO, Y. & HATTORI, Y. 2005 Curvature instability of a vortex ring. *J. Fluid Mech.* **526**, 77–115.

FUKUMOTO, Y. & MIYAZAKI, T. 1991 Three-dimensional distortions of a vortex filament with axial velocity. *J. Fluid Mech.* **222**, 369–416.

GUPTA, B. P. & LOEWY, R. G. 1974 Theoretical analysis of the aerodynamics stability of multiple, interdigitated helical vortices. *AIAA J.* **12**, 1381–1387.

HATTORI, Y. & FUKUMOTO, Y. 2009 Short-wavelength stability analysis of a helical vortex tube. *J. Fluid Mech.* **21**, 014104.

IVANELL, S., LEWEKE, T., SARMAST, S., QUARANTA, H. U., MIKKELSEN, R. F. & SØRENSEN, J. N. 2015 Comparison between experiments and large-eddy simulations of tip spiral structure and geometry. *J. Phys.: Conf. Ser.* **625**, 012018.

IVANELL, S., MIKKELSEN, R., SØRENSEN, J. N. & HENNINGSON, D. 2010 Stability analysis of the tip vortices of a wind turbine. *Wind Energy* **13**, 705–715.

VON KÁRMÁN, T. & RUBACH, H. 1912 Über den Mechanismus des Flüssigkeits- und Luftwiderstandes. *Phys. Z.* **13**, 49–59.

KERSWELL, R. R. 2002 Elliptical instability. *Annu. Rev. Fluid Mech.* **34**, 83–113.

KIDA, S. 1981 A vortex filament moving without change of form. *J. Fluid Mech.* **112**, 397–409.

KIDA, S. 1982 Stability of a steady vortex filament. *J. Phys. Soc. Japan* **51**, 1655–1662.

KOCH, C. R., MUNGAL, M. G., REYNOLDS, W. C. & POWELL, J. D. 1989 Helical modes in an acoustically excited round air jet. *Phys. Fluids* A **1**, 1443.

LAMB, H. 1932 *Hydrodynamics, § 156*. Cambridge University Press.

LEISHMAN, J. G. 2006 *Principles of Helicopter Aerodynamics*. Cambridge University Press.

LEISHMAN, J. G., BHAGWAT, M. J. & ANANTHAN, S. 2004 The vortex ring state as a spatially and temporally developing wake instability. *J. Am. Helicopter Soc.* **49**, 160–175.

LEVY, H. & FORSDYKE, A. G. 1927 The stability of an infinite system of circular vortices. *Proc. R. Soc. Lond.* A **114**, 594–604.

LEVY, H. & FORSDYKE, A. G. 1928 The steady motion and stability of a helical vortex. *Proc. R. Soc. Lond.* A **120**, 670–690.

LEWEKE, T. 2012 Dye visualization – a method for investigating biomechanical flows. *Curr. Pharm. Biotechnol.* **13**, 2141–2152.

LEWEKE, T., QUARANTA, H. U., BOLNOT, H., BLANCO-RODRÍGUEZ, F. J. & LE DIZÈS, S. 2014 Long- and short-wave instabilities in helical vortices. *J. Phys.: Conf. Ser.* **524**, 012154.

LEWEKE, T. & WILLIAMSON, C. H. K. 1998 Cooperative elliptic instability of a vortex pair. *J. Fluid Mech.* **360**, 85–119.

MEUNIER, P. & LEWEKE, T. 2003 Analysis and optimization of the error caused by high velocity gradients in particle image velocimetry. *Exp. Fluids* **35**, 408–421.

MEUNIER, P. & LEWEKE, T. 2005 Elliptic instability of a co-rotating vortex pair. *J. Fluid Mech.* **533**, 125–159.

NAUMOV, I. V., MIKKELSEN, R. F., OKULOV, V. L. & SØRENSEN, J. N. 2014 PIV and LDA measurements of the wake behind a wind turbine model. *J. Phys.: Conf. Ser.* **524**, 012168.

NEMES, A., LO JACONO, D., BLACKBURN, H. M. & SHERIDAN, J. 2015 Mutual inductance of two helical vortices. *J. Fluid Mech.* **774**, 298–310.

OHANIAN, C. V., MCCAULEY, G. J. & SAVAŞ, Ö. 2012 A visual study of vortex instabilities in the wake of a rotor in hover. *J. Am. Helicopter Soc.* **57**, 1–8.

OKULOV, V. L. & SØRENSEN, J. N. 2007 Stability of helical tip vortices in a rotor far wake. *J. Fluid Mech.* **576**, 1–25.

ROBINSON, A. C. & SAFFMAN, P. G. 1982 Three-dimensional stability of vortex arrays. *J. Fluid Mech.* **125**, 411–427.

ROSENHEAD, L. 1930 The spread in vorticity in the wake behind a cylinder. *Proc. R. Soc. Lond.* A **127**, 590–612.

ROY, C., LEWEKE, T., THOMPSON, M. C. & HOURIGAN, K. 2011 Experiments on the elliptic instability in vortex pairs with axial core flow. *J. Fluid Mech.* **677**, 383–416.

SAFFMAN, P. G. 1992 *Vortex Dynamics § 11.2*. Cambridge University Press.

SARMAST, S., DADFAR, R., MIKKELSEN, R. F., SCHLATTER, P., IVANELL, S., SØRENSEN, J. N. & HENNINGSON, D. S. 2014 Mutual inductance instability of the tip vortices behind a wind turbine. *J. Fluid Mech.* **755**, 705–731.

SELIG, M. S., GUGLIELMO, J. J., BROEREN, A. P. & GIGUERE, P. 1995 *Summary of Low-Speed Airfoil Data*. SoarTech.

SHERRY, M., NEMES, A., LO JACONO, D., BLACKBURN, H. M. & SHERIDAN, J. 2013 The interaction of helical tip and root vortices in a wind turbine wake. *Phys. Fluids* **25**, 117102.

SØRENSEN, J. N., MIKKELSEN, R., SARMAST, S., IVANELL, S. & HENNINGSON, D. 2014 Determination of wind turbine near-wake length based on stability analysis. *J. Phys.: Conf. Ser.* **524**, 012155.

SØRENSEN, J. N. & SHEN, W. Z. 2002 Numerical modelling of wind turbine wakes. *Trans. ASME J. Fluids Engng* **124**, 393–399.

STACK, J., CARADONNA, F. X. & SAVAŞ, Ö. 2005 Flow visualizations and extended thrust time histories of rotor vortex wakes in descent. *J. Am. Helicopter Soc.* **50**, 279–288.

VERMEER, L. J., SØRENSEN, J. N. & CRESPO, A. 2003 Wind turbine wake aerodynamics. *Progr. Aerosp. Sci.* **39**, 467–510.

WALTHER, J. H., GUÉNOT, M., MACHEFAUX, E., RASMUSSEN, J. T., CHATELAIN, P., OKULOV, V. L., SØRENSEN, J. N., BERGDORF, M. & KOUMOUTSAKOS, P. 2007 A numerical study of the instability of helical vortices using vortex methods. *J. Phys.: Conf. Ser.* **75**, 012034.

WIDNALL, S. E. 1972 The stability of a helical vortex filament. *J. Fluid Mech.* **54**, 641–663.

WIDNALL, S. E., BLISS, D. B. & ZALAY, A. 1971 Theoretical and experimental study of the instability of a vortex pair. In *Aircraft Wake Turbulence and its Detection* (ed. J. H. Olsen, A. Goldberg & M. Rogers), pp. 305–338. Plenum.